

## Article

# Effect of the Calcination Temperature of $\text{LaNiO}_3$ on the Structural Properties and Reaction Performance of Catalysts in the Steam Reforming of Methane

Yujie Wang, Shuairan Qian, Yuxin Chen, Binhang Yan  and Yi Cheng \*

Department of Chemical Engineering, Tsinghua University, Beijing 100084, China

\* Correspondence: yicheng@tsinghua.edu.cn or yicheng@mail.tsinghua.edu.cn

**Abstract:** The steam reforming of methane (SRM) reaction is a significant process for efficient syngas generation and for promising distributed hydrogen production. In this work, a series of  $\text{LaNiO}_3$  oxides were prepared using the Pechini method, calcined from 600 °C to 900 °C and tested for the SRM reaction. Fresh, reduced, and used samples were characterized using STA-MS-FTIR, in situ and ex situ XRD,  $\text{N}_2$  physical adsorption,  $\text{H}_2$ -TPR, TEM, TPO, and Raman. The results show that  $\text{LaNiO}_3$  begins to crystallize at about 550 °C, and the increase in calcination temperature results in the following differences in the properties of the  $\text{LaNiO}_3$  samples: larger  $\text{LaNiO}_3$  grains, smaller specific surface area, higher reduction temperature, smaller  $\text{Ni}^0$  grains reduced from the bulk phase, and stronger metal–support interaction. The maximum  $\text{CH}_4$  conversion could be achieved over  $\text{LaNiO}_3$  calcinated at 800 °C. In addition, the effect of steam-to-carbon ratio (S/C) on the performance of the SRM reaction was studied, and a S/C of 1.5 was found to be optimal for  $\text{CH}_4$  conversion. Too strong a metal–support interaction and too much unreacted steam causes a loss of catalytic activity. Finally, it was also proved using TPO and Raman that an increase in calcination temperature improves the carbon deposition resistance of the catalyst.

**Keywords:** steam reforming of methane; perovskite;  $\text{LaNiO}_3$ ; Pechini method; calcination temperature



**Citation:** Wang, Y.; Qian, S.; Chen, Y.; Yan, B.; Cheng, Y. Effect of the Calcination Temperature of  $\text{LaNiO}_3$  on the Structural Properties and Reaction Performance of Catalysts in the Steam Reforming of Methane. *Catalysts* **2023**, *13*, 356. <https://doi.org/10.3390/catal13020356>

Academic Editors: Hugo de Lasa and Mohammad Mozahar Hossain

Received: 26 December 2022

Revised: 29 January 2023

Accepted: 3 February 2023

Published: 6 February 2023



**Copyright:** © 2023 by the authors. Licensee MDPI, Basel, Switzerland. This article is an open access article distributed under the terms and conditions of the Creative Commons Attribution (CC BY) license (<https://creativecommons.org/licenses/by/4.0/>).

## 1. Introduction

Due to the continuous exploration of shale gas, combustible ice, and other natural gas (NG) resources, as well as the established mature infrastructure for the utilization of NGs, the reaction process of the steam reforming of methane still plays an important role in both the conventional manufacturing of syngas for subsequent liquid hydrocarbons and chemicals, and distributed hydrogen production with a combined use of fuel cells. Nickel-based catalysts are most commonly used for the SRM reaction because of their low cost, wide availability, and high activity comparable to noble metals. However, this type of catalyst is easily deactivated on account of sintering and/or carbon deposition, especially at a high reaction temperature [1–3]. Therefore, excessive steam is generally added to reduce or prevent coke deposition in industry, which leads to more energy input for water vaporization and water resource consumption. Thus, it is necessary to develop catalysts with a higher activity and less carbon deposition at lower S/C.

In addition to conventional catalysts, perovskite-type oxides (PTOs) have been widely used in a number of chemical reactions in recent years, including environmental catalysis [4], oxidation reactions (for CO and hydrocarbon) [5–7], reduction reactions (mainly for NO) [8–10], electrocatalysis as anode materials in solid oxide fuel cells (SOFCs) [11], and photoelectric conversion catalysis [12]. Owing to their excellent catalytic activity in reforming reactions, this type of oxide, with the general formula of  $\text{ABO}_3$ , has also served as the precursor for various reactions used to produce syngas [13–20] by generating well-defined crystalline oxide and subsequent highly dispersed metal particles through controlled exsolution from the bulk phase. In  $\text{ABO}_3$ , the B-site is usually occupied by a

catalytically active transition metal, while the A-site metals are mainly alkali, alkaline earth, and rare earth metals that are related to catalyst stability and that can interact with B-site elements to alter catalytic performance [20,21]. In addition to simple perovskite-type oxides, partially substituted PTOs have been employed to favor the interaction between different metallic species and between reduced metal particles and metal support oxides [22–27]. For example, Co could be inserted into  $\text{LaNiO}_3$ , and Ni-Co alloy is produced after  $\text{LaNi}_{1-x}\text{Co}_x$  is reduced by  $\text{H}_2$ , which promotes a high metal dispersion on the  $\text{La}_2\text{O}_3$  support and better catalytic stability [28–31]. Some researchers have also found that Ni catalysts generated from the ex-solution of perovskite-supported metal, such as  $\text{LaMnO}_3$ ,  $\text{LaFeO}_3$ , and  $\text{ATiO}_3$  (A=Ca, Sr, and Ba), showed superior resistance against coke formation in reforming reactions because the metal cations could reversibly enter the perovskite lattice to maintain high metal dispersion [32–37].

$\text{LaNiO}_3$ , as a typical perovskite-type oxide applied in reforming reactions, has been prepared using various methods, including solid state reaction, solution combustion, the Pechini method, the co-precipitate method, the hydrothermal method, the spray pyrolysis method, and so on [11]. Among these preparation approaches, the Pechini method is highly popular due to its simple operational procedure, controllable stoichiometry, high product purity, and strong reproducibility. Hence, it is employed to obtain the final  $\text{LaNiO}_3$  oxides herein. No matter what preparation method is adopted, the acquisition of the perovskite phase is the last step and the calcination temperature is the most critical process parameter. It has been reported in several studies that  $\text{LaNiO}_3$  exhibits a varying catalytic performance in reactions resulting from different calcination temperatures, which is induced by the different structures of calcinated and final products [13,15,38–40]. A study from the research group of Lina [41] has shown that calcination temperature would influence the Ni dispersion, metal–support interaction, and surface oxygen species of  $\text{LaNiO}_3$ . Daniela and coworkers [42] have suggested that some microstructural and superficial features, such as the  $\text{Ni}^{3+}/\text{Ni}^{2+}$  ratio and anionic vacancy presence, vary as a function of the calcination temperature of  $\text{LaNiO}_3$ . A study by Sang has shown that the most suitable calcination temperature of  $\text{LaNiO}_3$  in the SRM reaction was 700 °C, but the influence of calcination temperature was not discussed in depth. Thus, no systematic and comprehensive study on  $\text{LaNiO}_3$  calcinated at different temperatures has been carried out in the SRM reaction so far. By changing the calcination temperature of the perovskite phase, this work brought in a temperature-programmed analysis of dry gel, including a thermal analysis and a phase analysis, investigated the structural changes of perovskite oxides related to the calcination temperature through a series of material characterizations, and determined the optimal treatment temperature of the preparation process considering the activity and resistance to carbon deposition in the SRM reaction.

## 2. Materials and Methods

### 2.1. Catalysts Preparation

A series of  $\text{LaNiO}_3$  samples were prepared through the Pechini method [39,43], and then calcinated at different temperatures. Stoichiometric nitrates including  $\text{La}(\text{NO}_3)_3 \cdot 6\text{H}_2\text{O}$  (Aladdin, 99.99% purity) and  $\text{Ni}(\text{NO}_3)_2 \cdot 6\text{H}_2\text{O}$  (Xilong Chemical engineering, 98% purity) were dissolved with deionized water and citric acid (CA, General-reagent, 99.5% purity) was added under magnetic stirring with the ratio of CA to total metal cations equal to 1.2. After stirring for 1 h, ethylene glycol (EG:CA = 1:1) was added to the above solution and the temperature of oil bath increased to 80 °C to promote chelation and polyester reaction. A sponge-like green gel was produced after 4 h treatment and transferred to a drying oven to dry at 110 °C overnight. Then, the obtained dry gel was crushed into powder and calcinated in a muffle furnace. At first, the temperature was raised to 400 °C with a heating rate of 5 °C/min, and kept for 2 h to promote the decomposition of organic components. Then, the temperature increased to various pre-set temperatures, including 600 °C, 700 °C, 800 °C and 900 °C, and maintained for 5 h to ensure the formation of perovskite-type oxides. The obtained perovskite oxides were denoted as LNO-C600, LNO-C700, LNO-C800

and LNO-C900, respectively. Such calcination temperature was selected on the basis of an analysis of the decomposition of the precursor in the air atmosphere.

## 2.2. Catalysts Characterization

After drying at 110 °C, the gel precursor was characterized with an STA-MS-FTIR (simultaneous thermal analysis mass spectrometer Fourier transform infrared spectrometer) connected system (STA449F3-QMS403C-VERTEX70V, from NETZSCH in Germany) to test weight change, heat effect, and burnt-off gas products with the increase in temperature. Approximately 12 mg dry gel was added to an alumina crucible and the temperature was increased from room temperature to 900 °C with a heating rate of 10 °C/min in air atmosphere. The flow rate of air was 50 mL/min. In the mass spectra, the ion current intensities at  $m/z = 18, 28, 30, 44$  and  $46$  were used to represent the concentrations of  $H_2O, CO, NO, CO_2,$  and  $NO_2,$  respectively. The absorbances at 1510, 2178, 1832, 2358, and  $3073\text{ cm}^{-1}$  in the FTIR spectra were selected to stand for the concentration of  $H_2O, CO, NO, CO_2,$  and  $NO_2,$  respectively.

In situ and ex situ X-ray diffraction (XRD) characterizations were carried out at a Bruker D8 ADVANCE diffractometer, using a Cu  $K\alpha$  radiation source ( $\lambda = 0.154\text{ nm}$ ), and diffraction patterns were collected from  $5^\circ$  to  $90^\circ$  with a pace of  $5^\circ/\text{min}$ . Samples could also be placed in an alumina sample holder with programmable heating in hydrogen or air atmosphere to conduct in situ XRD measurement, with the temperature ranging from room temperature to 850 °C (the heating rate of 12 °C/min). The gas flow rate of hydrogen or air could be controlled at 10 mL/min with a mass flowmeter controller. The phase of the samples was identified by searching the JCPDS database and comparing the obtained patterns. The Scherrer equation was utilized to calculate the average crystallite size, where the value of  $k$ , shape factor, was 0.9.

$N_2$  adsorption–desorption analyses were performed to measure the specific surface area of prepared samples using a physical adsorption instrument (QUADRASORB SI, from Quantachrome Instruments in America) at 77 K, and the samples were previously degassed in vacuum to remove water and organic impurities at 300 °C for 16 h. The relative pressure (denoted by  $P/P_0$ ) set for these measurements was 0.01–0.99. The BET (Brunauer-Emmett-Teller) model was used to calculate the specific surface area of the calcinated samples.

Temperature-programmed experiments including TPR and TPO were performed at a FTIR (Nicolet-is50, from Thermo Fisher Scientific in America) to detect the changes in  $H_2O$  or  $CO_2$  concentration as the temperature increased. A total of 50 mg fresh sample was loaded in a quartz-tube reactor with an inner diameter of 4 mm under atmospheric pressure and pretreated at 400 °C under 20 mL/min Ar for 30 min to remove water from the calcinated samples. Cooling down to room temperature, the gas was switched to a 20 mL/min  $H_2/Ar$  (20%) mixture gas to conduct the TPR process, and the absorbance at  $1510\text{ cm}^{-1}$  marking the evolution concentration of  $H_2O$  was recorded when the temperature increased from room temperature to 900 °C with the heating rate of 10 °C/min. A total of 5 mg of the used sample was used and the carbonate was removed at 700 °C in Ar with a flow rate of 20 mL/min for 60 min. After cooling down to room temperature, 20 mL/min air/Ar (50%) was employed to oxidize the carbon deposition possibly existing in the spent catalysts to produce the absorbance at  $2358\text{ cm}^{-1}$  involving  $CO_2$  when the temperature increased to 900 °C with the heating rate of 10 °C/min.

TEM (transmission electron microscopy) images and EDS (energy dispersive spectroscopy) element mappings were obtained using JEM-2010 (from JEOL in Japan) operating at 200 kV. Samples for TEM were prepared by dispersing the sample with ethanol in an ultrasonic bath for 30 min to achieve a homogeneous dispersion and evaporating a drop of suspension in a carbon-coated copper grid at 80 °C for 10 min before observation.

Raman spectra were collected on a Raman spectrometer (LabRam HR Evolution Raman Spectrometer, from HORIBA Jobin Yvon in France) using a He-Ne laser (532 nm, 2 mW) under ambient conditions to probe into the nature of carbon formed during the

SRM reaction, with the wavelength region scanned ranging from 1000 to 2000  $\text{cm}^{-1}$ . The integration time was 60 s for each spectrum.

### 2.3. Catalytic Performance Evaluation

The catalytic performance of  $\text{LaNiO}_3$  perovskite oxide, calcined at different temperatures, was tested for the SRM reaction. The reforming reaction was carried out in a continuous flow quartz-tube reactor with an inner diameter of 4 mm operated at atmospheric pressure. A certain amount of catalyst was loaded into a quartz reactor and fixed in place with quartz wool for each test. Before the reaction, the catalysts were reduced in situ in 10 mL/min  $\text{H}_2$  at 850 °C for 2 h. Next, the reactant of the  $\text{CH}_4/\text{H}_2\text{O}$  mixture was fed into the reactor at a flow rate of 10 mL/min of methane, with the S/C ratio ranging from 1 to 3. At the outlet of the reactor, unreacted steam was removed through a condenser, and the concentration of gaseous reaction products was analyzed online with a gas chromatograph (SHIMADZU 2010) equipped with a TCD and an FID.

## 3. Results and Discussion

### 3.1. Formation of $\text{LaNiO}_3$ upon Calcination of the Gel Precursor in Air

#### 3.1.1. The Thermal Decomposition Analysis of the Dry Gel

In order to analyze the changes in composition and phase of the gel precursor (after the drying step at 110 °C overnight) during calcination, the dry gel was tested using STA-MS-FTIR in air atmosphere to obtain information including weight loss, thermal effect, and volatilized and/or decomposed gas products with the increase in temperature, which were helpful to clarify the physical or chemical processes occurring at different temperature scopes, and preliminarily determine the appropriate calcination temperature program.

The simultaneous thermal analysis results of TGA and DSC for dry gel prepared using the Pechini method are shown in Figure 1a, and the total weight loss of the gel is about 70% [44]. The Gram–Schmidt curve (GS curve for short) obtained through infrared spectroscopy is shown in Figure 1b, which shows that the total concentration of the evolving gas components over temperature corresponds significantly with the DTG curve, i.e., the first derivative of the TG curve. The components, including the  $\text{H}_2\text{O}$ ,  $\text{CO}_2$ ,  $\text{CO}$ ,  $\text{NO}_2$ , and  $\text{NO}$  that are possible in exhaust gas, were monitored using mass spectrometry and infrared spectroscopy. Since the information obtained using the two methods was fairly consistent, the concentration of gas products acquired through mass spectrometry was used representatively to reveal the thermal decomposition behaviors in Figure 2.

Considering the weight loss rate, thermal effect, and exhaust gas composition in each period, the thermal decomposition may be distinguished as follows (details tabulated in Table 1). The first thermal event mainly occurred up to 140 °C (endothermic peak in the DSC curve), with only water in the gas product. This stage is related to the removal of adsorbed water or coordinated water in the gel powder, accompanied by 2% weight loss [45,46]. In the second one, between 140 and 360 °C, the TGA curve became steep, representing a significant weight loss of ca. 38%, and  $\text{NO}$ ,  $\text{CO}_2$ , and  $\text{H}_2\text{O}$  were detected in the tail gas. No obvious  $\text{NO}_2$  and  $\text{CO}$  signals were detected, indicating that  $\text{NO}$  and  $\text{CO}_2$  are the main products of nitrate decomposition and organic oxidation, respectively. Therefore, the endothermic nitrate decomposition reaction and the exothermic organic oxidation process (mainly side-chain groups) occur simultaneously in this scope, but the overall effect is endothermic, which is due to the stronger reaction intensity of the former than that of the latter. The third process, from 360 to 570 °C, underwent a serious weight loss of ca. 28%, and the ionic strengths of the main products ( $\text{CO}_2$  and  $\text{H}_2\text{O}$ ) monitored through mass spectrometry increased greatly compared with the previous stages. This is attributed to the combustion of organic matter, along with an intense exothermic peak in the DSC curve [47]. The fourth period, from 570 to 700 °C, with an evolution of a small amount of  $\text{CO}_2$  as the only product, is ascribed to the decomposition of lanthanum oxycarbonate, which is the outcome of a basic lanthanum cation and  $\text{CO}_2$  from organic compounds oxidation [48]. In addition, the preliminary formation of the  $\text{LaNiO}_3$  crystalline phase took place during

this process [39], which could be verified in the following in situ XRD spectra of powder precursor in air atmosphere. Above 700 °C, there is no further weight loss [49], and no gaseous product has been detected using MS and FTIR, demonstrating that organic species have been burned out. In summary, the whole process consists in hydrate dehydration, the decomposition of anhydrous lanthanum citrate to an oxycarbonate, and a final phase transformation from lanthanum oxycarbonate to lanthanum-nickel oxide.

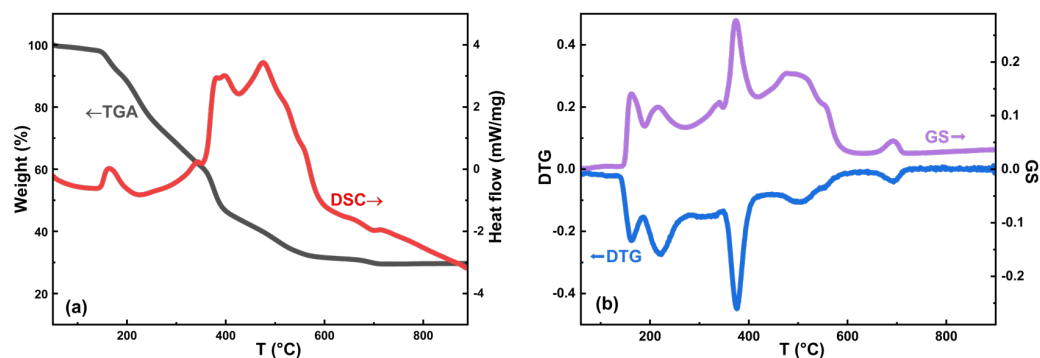


**Figure 1.** Simultaneous thermal analysis of gel precursor during heating in air: (a) TGA-DSC curve (endo down); (b) DTG-GS curve.

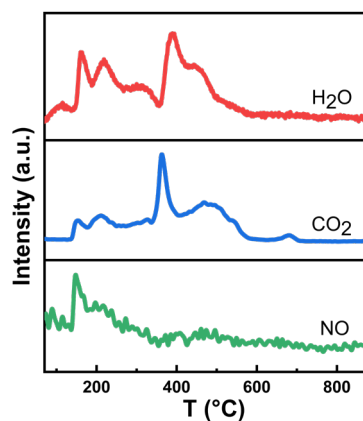


**Figure 2.** Evolution concentration of gas products with temperature during heating in air.

**Table 1.** The thermal events of the dry gel during heating in air atmosphere.

	T (°C)	Weight Loss (%)	Gas Products	Heat Effect	Thermal Events
Step 1	30–140	2	H <sub>2</sub> O	–	Dehydration
Step 2	140–360	38	CO <sub>2</sub> , H <sub>2</sub> O, NO	–	Decomposition of nitrate; oxidation of organic groups
Step 3	360–570	28	CO <sub>2</sub> , H <sub>2</sub> O	+	Oxidation of organic components; LaNiO <sub>3</sub> crystallization
Step 4	570–700	2	CO <sub>2</sub>	–	Decomposition of lanthanum oxycarbonate; LaNiO <sub>3</sub> crystallization
Step 5	700–900	0	None	–	LaNiO <sub>3</sub> crystallization

(+): exothermic; (–): endothermic.

As can be seen from the above analysis, the processes of nitrate decomposition and oxidative combustion of organic matter occur mostly within 400 °C. Thus, it is necessary to maintain a constant temperature at 400 °C for 2 h with the purpose of a full decomposition

and oxidation reaction. The intermediate phase, i.e., lanthanum oxycarbonate, is produced in the temperature-programmed process, and it is completely decomposed within 700 °C. As for more exact temperature when the LaNiO<sub>3</sub> crystalline phase appears, it needs to be further explored through an in situ XRD experiment in air atmosphere.

### 3.1.2. The Crystallization of LaNiO<sub>3</sub> Crystalline Phase

To complement the thermal analysis results obtained using STA-MS-FTIR, an in situ XRD test of the gel precursor was carried out in flowing air in a reaction chamber with temperature ranging from room temperature to 600 °C. The diffraction patterns of the powder precursor at different temperatures are illustrated in Figure 3. The gel shows up in an amorphous pattern until 450 °C, when some peaks begin to appear due to the crystalline phase, in accordance with ex situ XRD diffractograms in some other research [44,46]. The crystalline signals result from lanthanum oxycarbonate, i.e., La<sub>2</sub>O<sub>2</sub>CO<sub>3</sub>, which is a common type of oxide in the presence of basic cations in atmosphere containing CO<sub>2</sub>, mentioned in some earlier research on lanthanum oxide [45,47,48]. Continuing to heat up to 550 °C, weak diffraction peaks corresponding to the LaNiO<sub>3</sub> crystalline phase appear at 32.7 and 47.2° [44] and NiO at 37.3 and 43.3°. As the temperature continues to rise, La<sub>2</sub>O<sub>2</sub>CO<sub>3</sub> decomposes further to yield the final oxide LaNiO<sub>3</sub>. Since the complete decomposition of carbonate oxide and the crystallization of perovskite require a continuous high-temperature treatment of several hours, the temperature of the thorough disappearance of the La<sub>2</sub>O<sub>2</sub>CO<sub>3</sub> phase is not further studied here; we resort instead to ex situ XRD characterization, which is more realistic after consecutive calcination at a certain temperature.

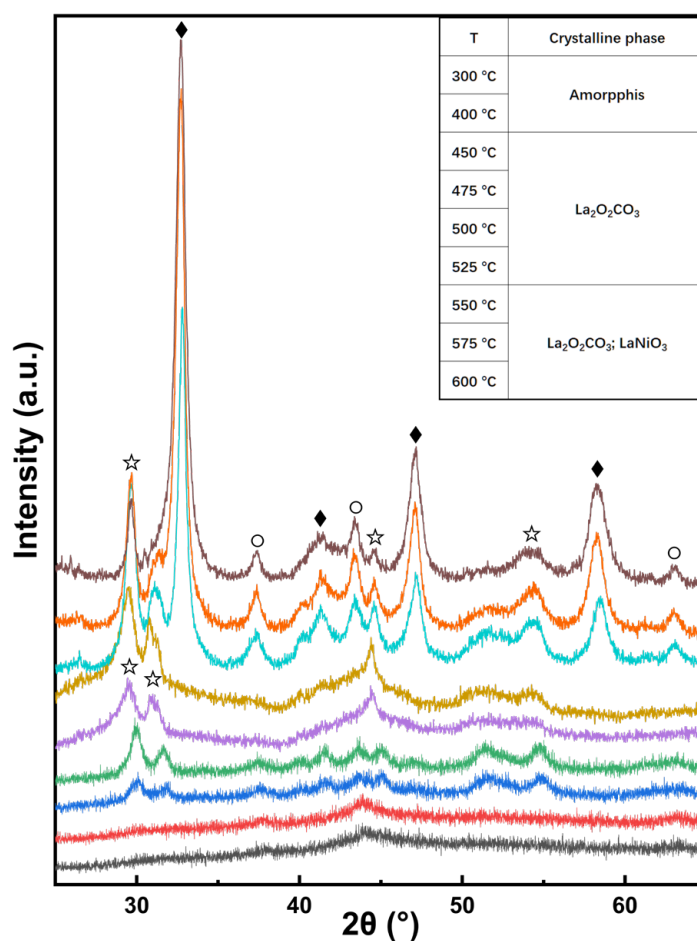


**Figure 3.** In situ XRD patterns of gel precursor during heating in air: diffractograms taken from 300 to 600 °C from bottom to top (◆-LaNiO<sub>3</sub>; ○-NiO; ☆-La<sub>2</sub>O<sub>2</sub>CO<sub>3</sub>).

With the aim of pure perovskite composition, the calcination temperature should be set above 600 °C at least according to Figure 3. Based on that, 600 °C, as a boundary temperature, was established as the lowest one used for calcination of LaNiO<sub>3</sub>. Considering also the STA-MS-FTIR results, which show that the decomposition process in fact proceeds until 700 °C, a series of calcination temperatures were chosen to prepare the catalysts.

### 3.2. Physical Properties of Calcinated LaNiO<sub>3</sub> Oxide

After analyzing the preparation process of the Pechini method, LaNiO<sub>3</sub> samples calcinated at different temperatures (600–900 °C) were characterized using XRD to investigate the effect of calcination temperature on the LaNiO<sub>3</sub> crystalline phase, with patterns shown in Figure 4. For samples treated at higher temperatures ( $\geq 700$  °C), only pure perovskite phase indexed perfectly to JCPDS No.33-0711 was detected, which also indicates the proper application of the synthesis method<sup>46</sup>. In addition to the perovskite phase, the LNO-C600 sample also shows a weak diffraction peak of NiO<sup>13</sup> marked with a hollow circle at 43.3° (indexed to JCPDS No.78-0643), demonstrating that part of the La and Ni components were not combined into the perovskite crystalline phase, and the intensity of the diffraction peak with burrs was relatively low, which reveals the poor crystallinity of oxide [39]. With the increase in calcination temperature, the peak of the perovskite structure was significantly enhanced, and also became sharper, which suggests more complete crystallization, that is, the structure of LaNiO<sub>3</sub> is more perfect [15]. Furthermore, the grain size of the LaNiO<sub>3</sub> crystalline phase can be calculated using the Scherrer equation based on the most intense peak of the XRD pattern at 32.7°. The results are summarized in Table 2, showing that the crystal size of LaNiO<sub>3</sub> increased from 10.0 to 17.9 nm with calcination temperature [46,50]. The calculated cell parameters of each sample are also shown in Table 2. It has been reported that unit cell volume is concerned with atomic distance and bond length. Therefore, it could be inferred that increased calcination temperature reduces the length of the La-O and Ni-O bonds, thus affecting the corresponding bond strength.

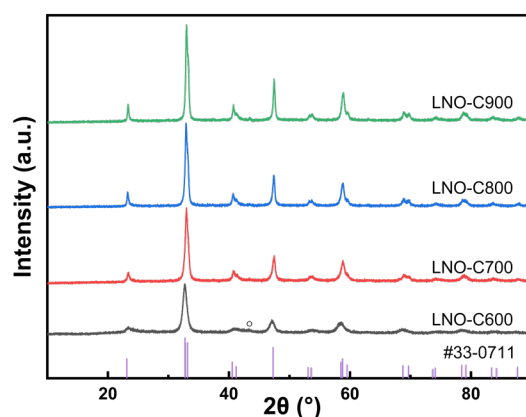


Figure 4. XRD patterns of LaNiO<sub>3</sub> samples calcined at different temperatures (○-NiO).

Table 2. Summary of significant properties of calcinated and reduced samples.

Sample	SSA <sub>BET</sub> /m <sup>2</sup> ·g <sup>-1</sup>	D(LaNiO <sub>3</sub> )/nm	Distorted Rhombohedral Symmetry			D(Ni <sup>0</sup> )/nm	T (Reduction Peak)/°C
			a/Å	c/Å	V/Å <sup>3</sup>		
LNO-C600	10.796	10.0	5.474	6.738	169.84	30.0	305; 349; 514
LNO-C700	8.033	13.9	5.453	6.636	169.20	26.5	370; 526
LNO-C800	4.579	15.8	5.440	6.585	168.79	22.8	387; 536
LNO-C900	2.544	17.9	5.430	5.579	168.15	19.8	387; 545

The above results indicate that the increased calcination temperature can promote the crystallization process of perovskite oxide and enhance the ionic bond strength of  $\text{LaNiO}_3$ . The higher the calcination temperature, the larger the crystal size of  $\text{LaNiO}_3$  [50,51].

The textural properties of fresh catalysts were studied using the  $\text{N}_2$  physical adsorption analysis shown in Figure 5. Type III adsorption isotherms, with Type H3 hysteresis during the desorption process, could be obtained in all the samples, indicating non-porous or macroporous materials. Consistent with the conclusions of related studies [15,39,52], the specific surface area of perovskite was generally less than  $10 \text{ m}^2 \cdot \text{g}^{-1}$ , due to the fact that high-temperature calcination is necessary for the crystallization of perovskite-type oxide. For the samples calcined at different temperatures, the specific surface area decreased markedly from  $10.796 \text{ m}^2 \cdot \text{g}^{-1}$  of LNO-C600 to  $2.544 \text{ m}^2 \cdot \text{g}^{-1}$  of LNO-C900 (in Table 2), which is attributed to particle sintering caused by higher temperature, corresponding with XRD characterization results in Figure 4.

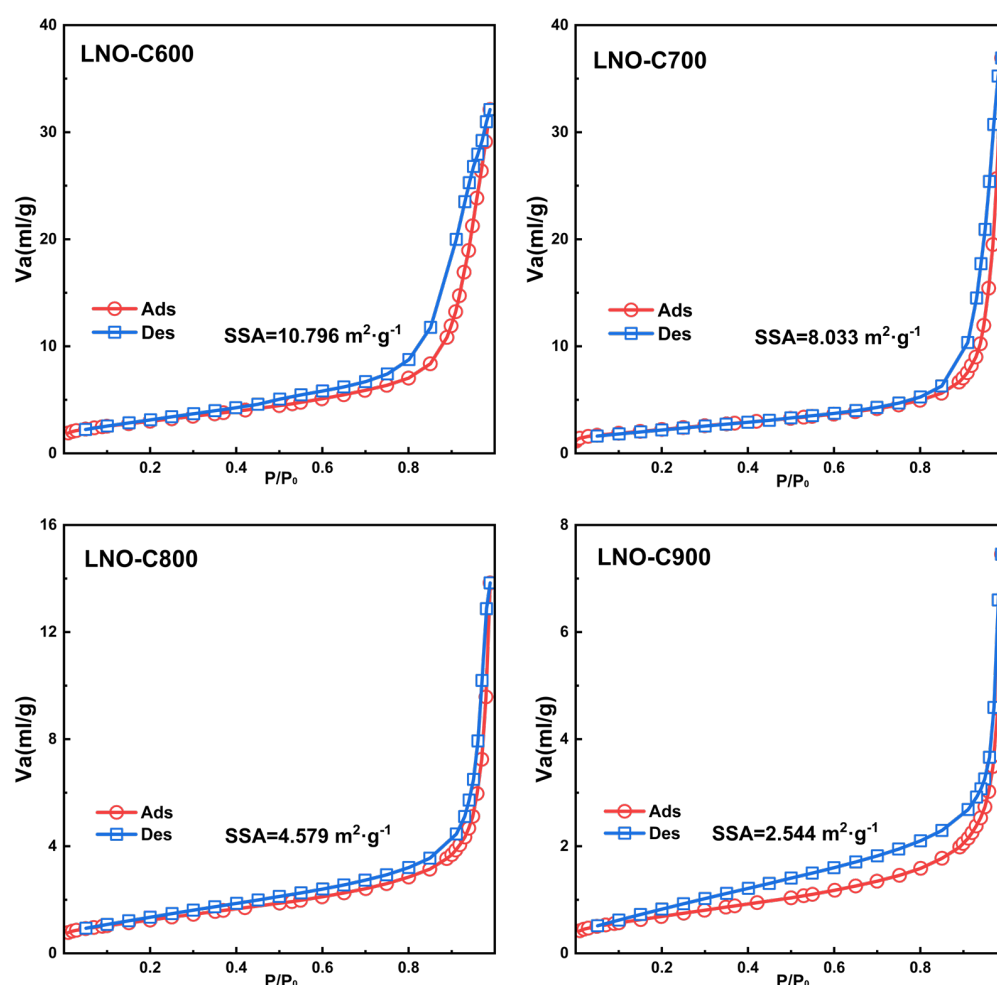


Figure 5.  $\text{N}_2$  adsorption–desorption isotherms of  $\text{LaNiO}_3$  samples calcined at different temperatures.

### 3.3. Reducibility of Calcinated $\text{LaNiO}_3$ Oxides

Since the active component of the SRM reaction is reduced nickel metal located on the surface of catalyst, the reductive activation of  $\text{LaNiO}_3$  should be completed in the reducing atmosphere before methane conversion, transforming perovskite into metal supported on oxide. Therefore, the crucial reduction properties of the  $\text{LaNiO}_3$  crystalline phase were studied using  $\text{H}_2$ -TPR and in situ XRD in  $\text{H}_2$  atmosphere [53,54], with the purpose of illuminating the reduction process and reduction results of samples obtained at different calcination temperatures.

The H<sub>2</sub>-TPR profiles of LaNiO<sub>3</sub> samples are shown in Figure 6, where LNO-C600 has three reduction peaks, while the samples calcinated at temperatures above 700 °C have two peaks. Referring to the XRD characterization of LNO-C600 and in situ XRD in air, it can be known that there is still a certain amount of NiO present in the sample after 600 °C calcination, which is not combined with the stoichiometrically corresponding La component. Thus, there is the reduction process of free NiO phase, corresponding to the reduction peak in the left, at about 300 °C [13,55]. The remaining two peaks are consistent with those of other samples calcined at higher temperatures, which are attributed to the reduction of LaNiO<sub>3</sub>, but the positions shift. To be specific, the higher the calcination temperature of LaNiO<sub>3</sub>, the higher the reduction temperature [56–58]. In terms of the high-temperature reduction peak of LaNiO<sub>3</sub>, the temperature varies from the 514 °C of LNO-C600 to the 526, 536, and 545 °C of LNO-C700, LNO-C800, and LNO-900, respectively, which demonstrates more the difficult reduction process of LaNiO<sub>3</sub> with the calcination temperature increasing. This phenomenon can be explained by the enhanced La-O-Ni ionic bond strength in the perovskite phase owing to the higher calcination temperature, deduced from the cell parameters of samples in XRD characterization, which makes it more difficult to extract Ni from bulk oxide.

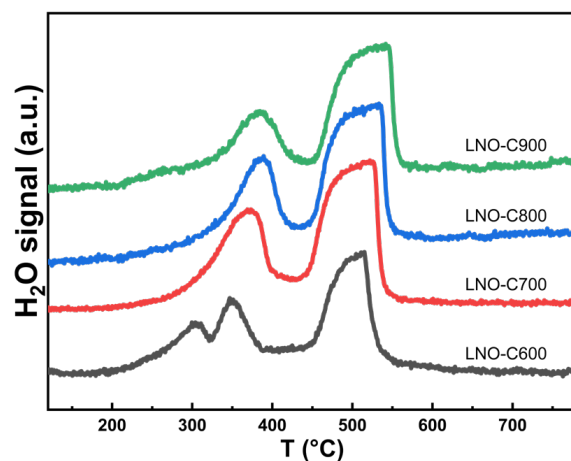
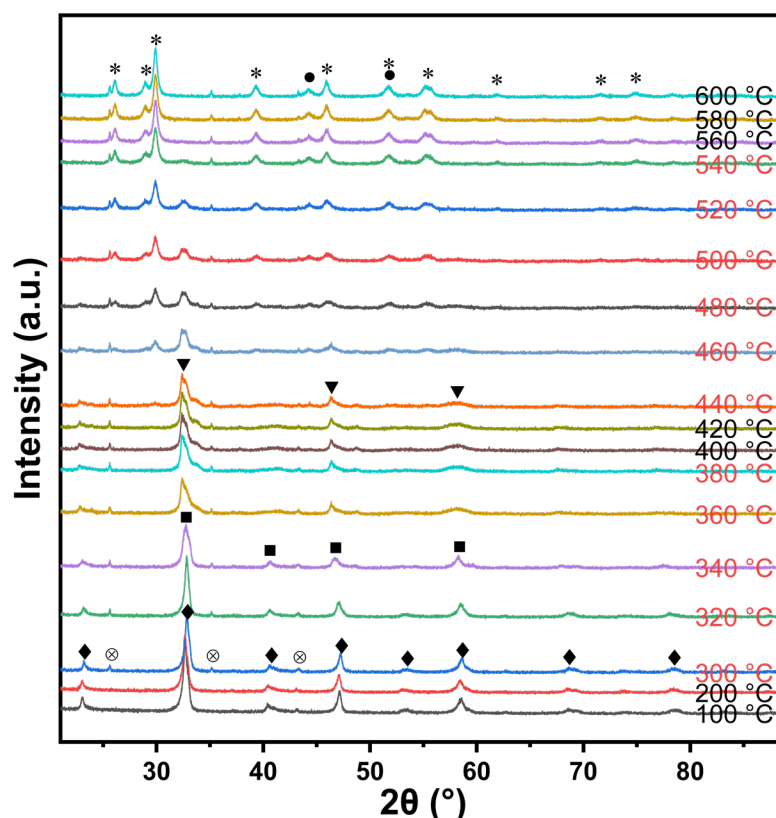
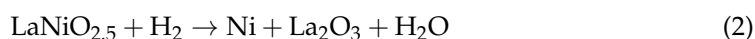
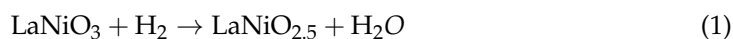


Figure 6. H<sub>2</sub>-TPR profiles of LaNiO<sub>3</sub> samples calcined at different temperatures.

Moreover, it can be concluded from the H<sub>2</sub>-TPR profiles that the reduction of the LaNiO<sub>3</sub> phase is completed through two steps: (i) the first reduction step at 250–430 °C; (ii) the second reduction step at 44–560 °C [59,60]. Moreover, the area of high-temperature reduction peaks is larger than that of the low-temperature reduction peak. The actual crystalline phase transition during the reduction process was investigated by following in situ XRD in H<sub>2</sub>. Taking the LNO-C800 sample as an example, XRD patterns during the reduction process in H<sub>2</sub> are collected, as shown in Figure 7, to learn about the transition temperature of the LaNiO<sub>3</sub> phase and the intermediate phase existing in the reduction process. The reduction process mainly occurs between 300 and 560 °C, and two steps of the process can be clearly observed from the evolution of the crystalline phase.

The first step (Equation (1)), located at 300–380 °C, is consistent with the temperature range of the low-temperature reduction peak of the H<sub>2</sub>-TPR profile. By comparing the crystal database, it can be obtained that the crystalline phases at 340 and 360 °C are LaNiO<sub>2.7</sub> (JCPDS No.37-0928) and LaNiO<sub>2.5</sub> (JCPDS No.82-0556) [52,61,62], respectively. Above 360 °C, the LaNiO<sub>2.5</sub> phase remains in spite of the increase in temperature [63,64]. In this step, Ni<sup>3+</sup> is reduced to Ni<sup>2+</sup>, and part of the lattice oxygen in the LaNiO<sub>3</sub> phase is consumed. The perovskite structure is still maintained, though the lattice arrangement is distorted by the oxygen vacancies in the bulk of the crystalline phase, which can be seen in the less intense and broader peaks than that of fresh samples without reduction. Moreover, it can be observed that the main diffraction peak of LaNiO<sub>3-δ</sub> shifts to the left, which corresponds to the decrease in diffraction angle 2θ. According to the Bragg equation,

the interplanar crystal spacing becomes larger, attributable to the fact that the ion radius of Ni becomes larger and the unit cell expands, resulting from a partial reduction by receiving electrons. The second step (Equation (2)), from 440 °C to 560 °C, can be assigned to the high-temperature reduction peak in the H<sub>2</sub>-TPR profile. The diffraction pattern does not change until 440 °C, prior to which the previous LaNiO<sub>2.5</sub> crystalline phase is preserved. With the increase in temperature, and the continuing decrease in the diffraction peak intensity of the distorted perovskite phase, the Ni metal and La<sub>2</sub>O<sub>3</sub> oxide phase appears. By 560 °C, the perovskite phase disappears completely, and the activated nickel metal supported on La<sub>2</sub>O<sub>3</sub> is obtained.



**Figure 7.** In situ XRD patterns of LNO-C800 during heating in H<sub>2</sub> atmosphere: diffractograms taken from 100 °C to 600 °C from bottom to top (◆-LaNiO<sub>3</sub>; ■-LaNiO<sub>2.7</sub>; ▼-LaNiO<sub>2.5</sub>; ●-Ni; \*-La<sub>2</sub>O<sub>3</sub>; ⊗-intrinsic signal from instrument).

After the reduction process is completed, the diffraction peak of the pattern becomes more intense and sharper (not listed) with the increase in the temperature, indicating that the crystalline phase is more perfect and the crystal size increases to a certain extent [61]. As the temperature rises from 600 to 850 °C, the crystal size of Ni<sup>0</sup> (calculated according to the main peak at 44.3°) increases from 15.0 nm to 23.0 nm, as shown in Figure 8.

### 3.4. Characterization of Reduced Catalysts

It is necessary to explore crystalline phase and morphology of reduced catalyst by XRD and TEM characterization as the LaNiO<sub>3</sub> sample needs to be activated in a pure hydrogen atmosphere at 850 °C for 2 h before the catalytic reforming reaction. The XRD patterns of each catalyst after reduction are illustrated in Figure 9. All the samples appear as Ni (JCPDS No.04-0850), La(OH)<sub>3</sub> (JCPDS No.36-1481), and La<sub>2</sub>O<sub>3</sub> (JCPDS No.74-2430) after reduction [65,66]. Comparing the diffraction peaks of Ni crystal from different samples

after reduction, it can be concluded that the higher the calcination temperature of  $\text{LaNiO}_3$ , the smaller the  $\text{Ni}^0$  crystal size obtained after reduction [38], as listed in Table 2.

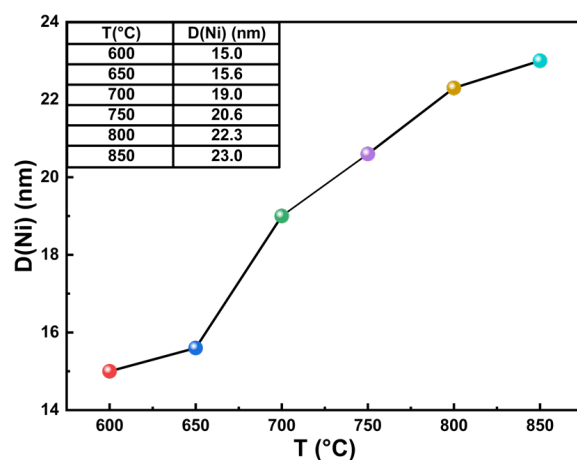


Figure 8. Evolution of nickel crystal size during heating in  $\text{H}_2$  atmosphere.

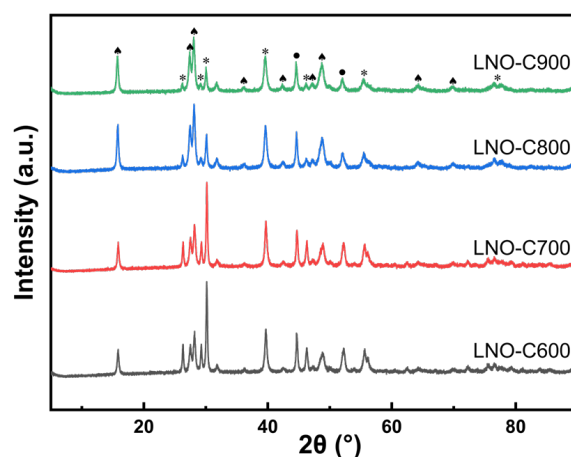


Figure 9. XRD patterns of different samples reduced in  $\text{H}_2$  at  $850\text{ }^\circ\text{C}$  (♠- $\text{La}(\text{OH})_3$ ; ●- $\text{Ni}$ ; \*- $\text{La}_2\text{O}_3$ ).

The aforementioned  $\text{H}_2$ -TPR profiles reveal the gradual reduction difficulty of the fresh sample with the higher calcination temperature, which is significant for elucidating this phenomenon. The higher calcination temperature of  $\text{LaNiO}_3$  makes it more difficult to extract Ni from bulk oxide, and the metal–support interaction of the catalysts obtained after reduction also becomes stronger [67,68]. The resistance of dissolving out from the bulk can keep Ni grains from aggregating in a degree, so that smaller grains can be obtained.

Transmission electron microscopy (TEM) was used to observe the morphology of reduced catalysts, and nearly spherical Ni crystalline grains, supported on layered  $\text{La}_2\text{O}_3$  support [69,70], were obtained for each catalyst after reduction, as shown in Figure 10. Clear lattice fringes can be observed through high-resolution TEM images in Figure 11a, and the crystal plane spacing proves that a large amount of the spreading phase was  $\text{La}_2\text{O}_3$  oxide, while the spherical structure in the edge was Ni metal crystal, as shown in Figure 11b. EDS mappings in Figure 12 also verify the catalyst system where Ni is loaded on the oxide of La after reduction. There is a highly consistent distribution in terms of La and O elements, while Ni and O do not coincide. The La element displays continuous distribution with a larger area, and Ni element appears as granular dispersion.

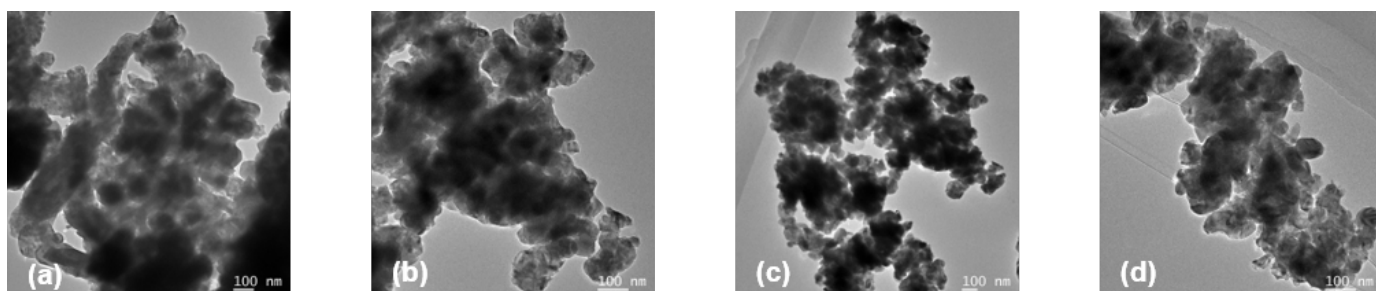


Figure 10. TEM images of reduced catalysts: (a) LNO-C600; (b) LNO-C700; (c) LNO-C800; (d) LNO-C900.

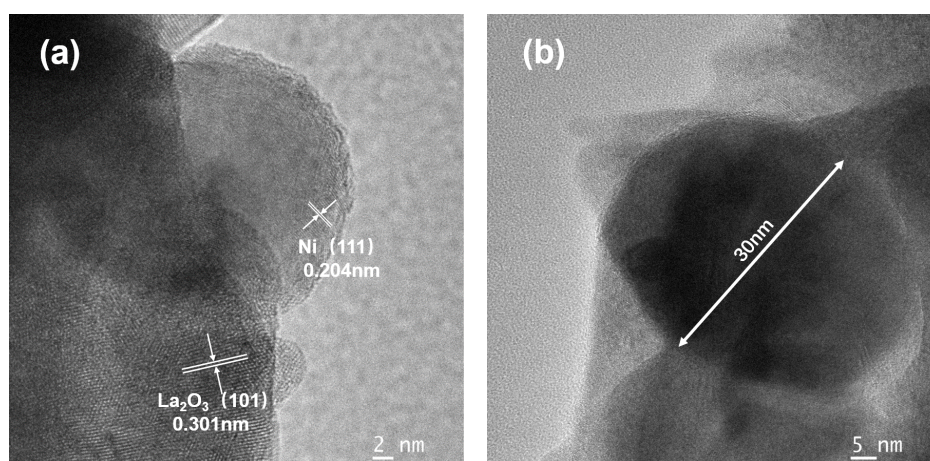


Figure 11. Local Ni crystal grain supported on  $\text{La}_2\text{O}_3$  oxide of reduced LNO-C800 catalyst: (a) the lattices of Ni crystal and  $\text{La}_2\text{O}_3$  support; (b) spherical Ni metal crystal grain.

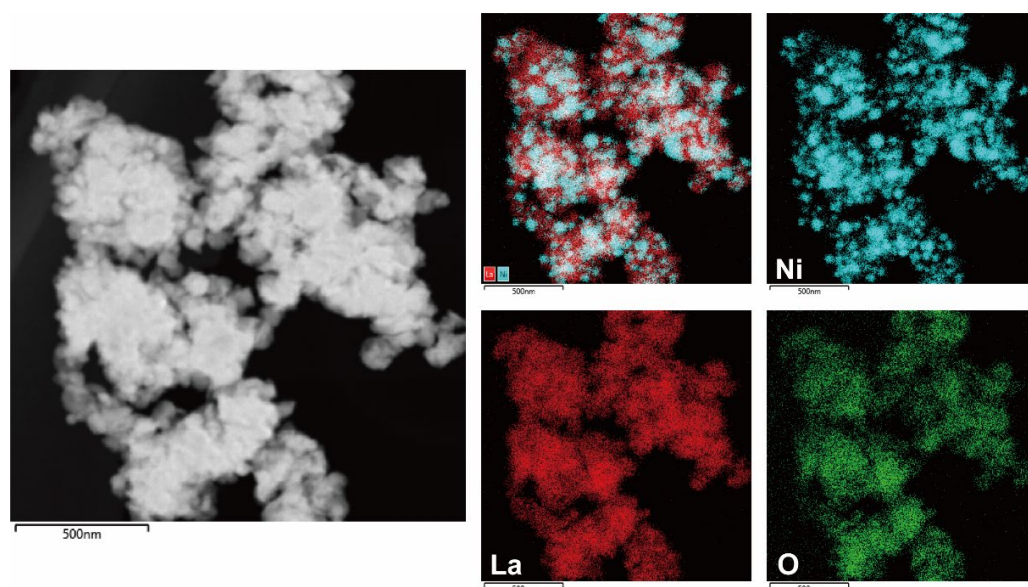
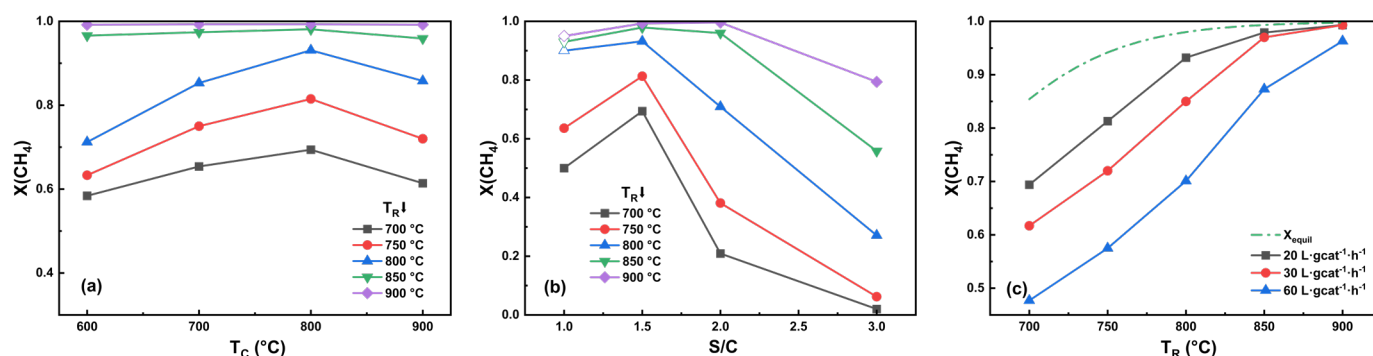


Figure 12. EDS mappings of reduced LNO-C800 catalyst involving La, Ni, and O elements.

### 3.5. Reaction Performance of Reduced $\text{LaNiO}_3$ Samples

The activity of  $\text{LaNiO}_3$  samples previously calcined at different temperatures was tested after in situ reduction at  $850\text{ }^\circ\text{C}$  for 2 h in  $\text{H}_2$ . Firstly, the influence of the calcination temperature ( $T_C$ ) of  $\text{LaNiO}_3$  was studied. The reaction temperature ( $T_R$ ) varied from  $700$  to  $900\text{ }^\circ\text{C}$ , and each  $T_R$  was held for 3 h, with a steam-to-carbon ratio ( $S/C$ ) equal to 1.5. The reactor was first set at  $900\text{ }^\circ\text{C}$ , and the system could reach the steady state 20 min

after the reactants were fed into the reactor. Then, the reaction performance data would be recorded. Moreover, 10 min for system stabilization were also allowed each time when the reactor temperature was switched. Figure 13a shows the relationship between catalyst activity and  $T_C$  under different  $T_R$ . For each catalyst, the higher the  $T_R$ , the higher the methane conversion [15,71,72]. The conversion reached more than 95% at 850 °C, and nearly complete conversion could be acquired at 900 °C. At the same  $T_R$ , elevated  $T_C$ , ranging from 600 to 800 °C, resulted in a gradually increased methane conversion, which reached its maximum when  $\text{LaNiO}_3$  was calcinated at 800 °C. The reaction performance improved more remarkably with the increase in  $T_C$  when  $T_R$  was less than 800 °C. Nevertheless, continuing to raise  $T_C$  to 900 °C, methane conversion decreased, and the reduction in activity was more notable at lower  $T_R$  (below 800 °C). As the calcination temperature increased, the reduced Ni particle became smaller and smaller. As has been studied in the literature, smaller Ni grains can increase the activation rate of methane, which has a significant impact on the activity of the catalyst [73–76]. Moreover, it is generally accepted that steam is activated either through Ni crystal grains or by oxide support [73,77]. Then, the differences in calcination temperature will also alter the interaction between the support and the active component of the reduced catalyst, which facilitates the overflow of oxygen species from  $\text{La}_2\text{O}_3$  to Ni [73,78,79]. The good hygroscopicity [80] of the La element makes it easier for it to adsorb and activate steam, and produce reactive oxygen species including hydroxyl and atomic oxygen, which can be delivered to some adjacent Ni clusters. In addition, a strong interaction would cause an unbalanced oxygen species supply against the methane dissociation rate and a reduction in catalytic activity [68,81].



**Figure 13.** (a) The relationship between methane conversion and the  $T_C$  of  $\text{LaNiO}_3$  at different  $T_R$ . Reaction conditions:  $T_R$  from 700 to 900 °C,  $S/C = 1.5$ , atmospheric pressure,  $\text{GHSV} = 20 \text{ L} \cdot \text{gcat}^{-1} \cdot \text{h}^{-1}$ ; (b) the relationship between the methane conversion of reduced LNO-C800 and  $S/C$  at different  $T_R$ . Reaction conditions:  $T_R$  from 700 to 900 °C, atmospheric pressure,  $\text{GHSV} = 20 \text{ L} \cdot \text{gcat}^{-1} \cdot \text{h}^{-1}$ ; (c) the relationship between the methane conversion of reduced LNO-C800 and reaction space velocity at different  $T_R$ . Reaction conditions:  $T_R$  from 700 to 900 °C, atmospheric pressure,  $S/C = 1.5$ .

Then, with  $S/C$  ranging from 1 to 3, an activity evaluation for the reduced catalyst of LNO-C800 was performed and the results obtained at different  $T_R$  are shown in Figure 13b. It can be seen that 1.5 is the optimal  $S/C$  ratio, but the composition of the reactants consistent with the stoichiometry of the SRM reaction equation could not provide the highest conversion. The  $S/C$  continued to increase from 1.5 to 2.0, and the methane conversion decreased to various degrees at different  $T_R$ . At relatively lower  $T_R$ , the activity decreased more rapidly, which was caused by the oxidation effect of Ni through excess steam, verified in the XRD characterization of used catalyst in the following. If the  $S/C$  continues to increase, methane conversion will further decline. Compared with traditional supported nickel-based catalysts, this type of catalyst derived from  $\text{LaNiO}_3$  precursor requires a lower  $S/C$  to achieve optimal reforming reaction activity, which may also depend on the hygroscopicity and alkalinity of the  $\text{La}_2\text{O}_3$  support oxide [78,80].

Finally, the effect of space velocity on methane conversion was studied by changing the catalyst loading amount to 25 mg, 50 mg, and 75 mg, respectively, and the results are illustrated in Figure 13c. At the space velocity of  $20 \text{ L}\cdot\text{gcat}^{-1}\cdot\text{h}^{-1}$ , the methane conversion close to the thermodynamic equilibrium can be reached when the reaction temperature is higher than  $800 \text{ }^\circ\text{C}$ , while at a relatively low temperature (lower than or equal to  $750 \text{ }^\circ\text{C}$ ), the reaction performance is greatly limited by kinetics [82,83]. When the space velocity is increased to 30 and  $60 \text{ L}\cdot\text{gcat}^{-1}\cdot\text{h}^{-1}$ , the methane conversion decreases to an extent.

### 3.6. Spent Catalysts Characterization

#### 3.6.1. Effect of S/C on Crystalline Phase

The reduced catalysts from the LNO-C800 sample after the SRM reaction at different S/C were characterized using XRD. As shown in Figure 14, when stoichiometric reactants were fed, the support appeared as  $\text{La}_2\text{O}_2\text{CO}_3$  (JCPDS No. 37-0804), and the Ni element only existed in the metallic state. When S/C was 2, the crystalline phases of support included  $\text{La}_2\text{O}_2\text{CO}_3$  and  $\text{La}(\text{OH})_3$ , and NiO also began to emerge. With the increase in S/C to 3,  $\text{La}(\text{OH})_3$  mainly existed in the support, accompanied by a small amount of  $\text{La}_2\text{O}_3$ , and the diffraction peak intensity of NiO was further strengthened. The more intense peak of NiO confirms that the increase in S/C causes the oxidation of the metallic active component of Ni in the catalyst, and a growing number of NiO results in the reduction in the reaction activity at higher S/C. In addition, when S/C is lower and the residual steam in the reactor is less,  $\text{La}_2\text{O}_3$  tends to combine with  $\text{CO}_2$  in the product to form oxycarbonate  $\text{La}_2\text{O}_2\text{CO}_3$ . By contrast, a higher S/C could make  $\text{La}_2\text{O}_3$  transform into  $\text{La}(\text{OH})_3$ .

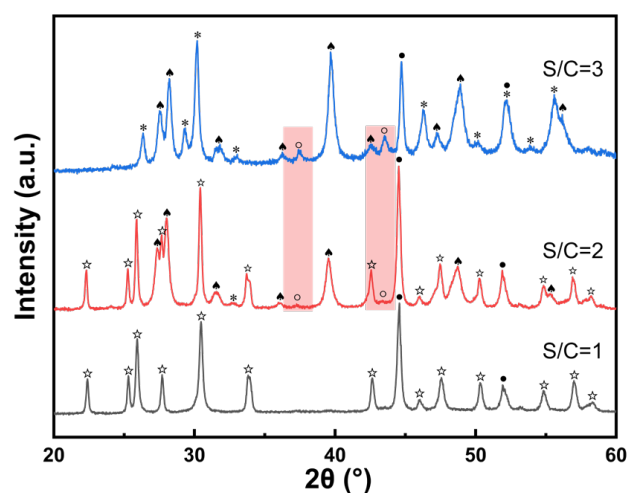


**Figure 14.** XRD patterns of used LNO-C800 samples after reaction at different S/C (●-Ni; ○-NiO; ☆- $\text{La}_2\text{O}_2\text{CO}_3$ ; ▲- $\text{La}(\text{OH})_3$ ; \*- $\text{La}_2\text{O}_3$ ).

#### 3.6.2. Resistance to Carbon Deposition

With S/C equal to 1, the catalyst (60–80 mesh) was used to carry out the SRM reaction for 4 h at  $850 \text{ }^\circ\text{C}$  and  $60 \text{ L}\cdot\text{gcat}^{-1}\cdot\text{h}^{-1}$ . The study of the nature and amount of the carbonaceous deposition formed in reforming process was conducted with the approaches including the TEM, Raman, and temperature-programmed oxidation (TPO) experiments.

TEM was used to reveal the morphology of the carbonaceous deposition forming at S/C = 1, as shown in Figure 15. Fibrous carbon deposition was formed [84,85], and a large number of Ni particles were lifted from the support, isolated from the main catalyst system. The filamentous carbon material appeared as a layered graphene structure on either side or around the nickel particles<sup>13</sup>.

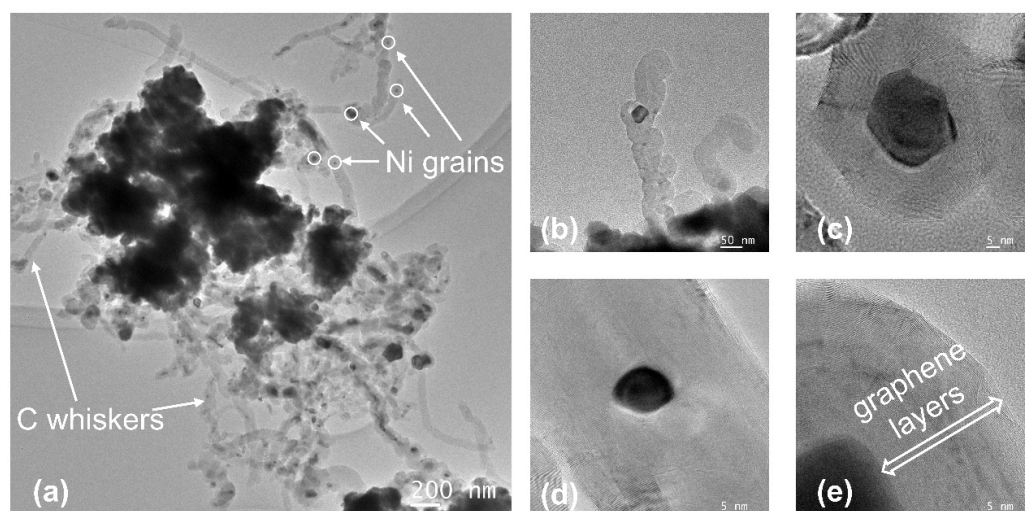


**Figure 15.** TEM images of carbon deposition generated through the SRM reaction of LNO-C800 at S/C = 1: (a) catalyst and coexisting filamentous carbon deposition; (b,c) Ni grains lifted from the support; (d,e) graphene layers of graphite-like structures.

Raman spectra were used to elucidate the quality of the carbon deposition, where  $I_D/I_G$  ratios (standing for the Raman intensities of D-band and G-band peaks) could show amorphous degrees of carbon materials. Figure 16a reveals that the D peak and G peak signals appeared for each catalyst after the reaction [86,87], and the amorphous degree of graphite-carbon was about 0.4. The carbon deposition of LNO-C600 was the most serious, followed by LNO-C700, and the other two samples almost had some carbon deposition. A similar tendency was also obtained in the TPO experiment (in Figure 16b) [88–90]. LNO-C600 had the strongest  $\text{CO}_2$  evolution signal, at about 610 °C, compared with a weaker signal from LNO-C700 at about 580 °C. However, LNO-C800 and LNO-C900 had very weak evolution peaks at about 500 °C. Quantitative carbon deposition can be obtained by integrating  $\text{CO}_2$  signal curves, and the results are summarized in Table 3.

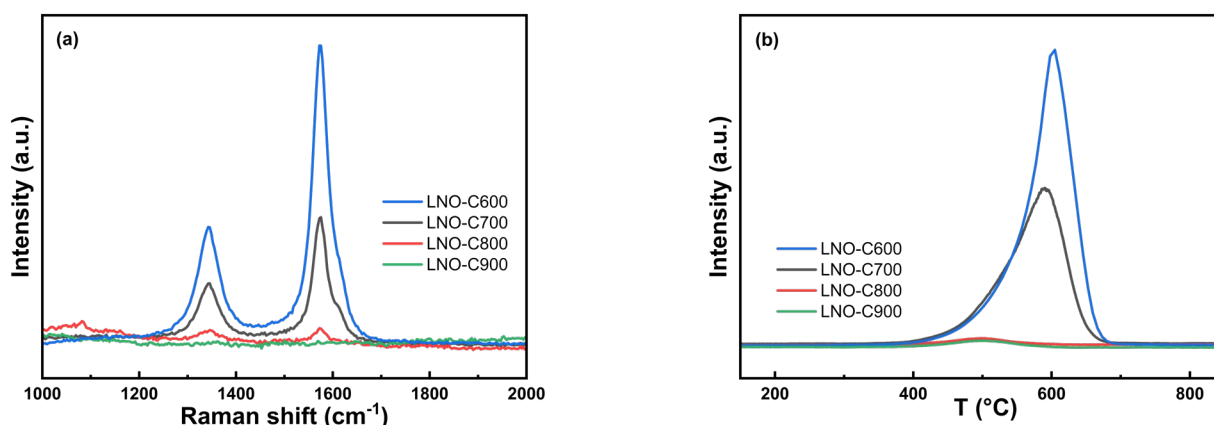


**Figure 16.** Comparison of the carbon deposition of different samples after 4 h of SRM reaction under the condition of S/C = 1: (a) Raman; (b) TPO.

The Raman and TPO experiments demonstrate that the carbon deposition resistance of catalysts is improved with the increase in the calcination temperature of dry gel to prepare  $\text{LaNiO}_3$ , and the carbon deposition is very low in terms of the calcination temperature of 800 °C and above. The stability of the catalyst depends on the size of the metal particle, the nature of support dispersing metal particles, and the interaction between the metal phase and the support [91]. According to the above studies, the higher calcination temperature can result in both smaller Ni grains and stronger interactions between Ni and  $\text{La}_2\text{O}_3$ . The

latter brings more reactive oxygen species to Ni grains that are conducive to the elimination of carbon deposition [92,93]; there is therefore a positive correlation between calcination temperature and resistance to carbon deposition [81].

**Table 3.** Carbon deposition of different catalysts after 4 h of the SRM reaction under the condition of S/C = 1.

Catalysts	mg C/mg Catalyst (%)	T (Carbon Elimination Peak)/°C
LNO-C600	18.56	610
LNO-C700	9.85	580
LNO-C800	0.56	498
LNO-C900	0.50	497

#### 4. Conclusions

The LaNiO<sub>3</sub> precursor was prepared using the Pechini method and reduced before the SRM reaction to form a supported Ni/La<sub>2</sub>O<sub>3</sub> catalyst. The effect of the calcination temperature of LaNiO<sub>3</sub> on the structural properties and catalytic performance of samples for the SRM reaction was analyzed. Firstly, the formation of LaNiO<sub>3</sub> on the calcination of the gel precursor in air was investigated with STA-IR-MS and in situ XRD, providing the information which elaborates thermal events at different temperatures, the existence of a La<sub>2</sub>O<sub>3</sub>CO<sub>3</sub> intermediate appearing about at 450 °C, and the initial crystallization temperature of LaNiO<sub>3</sub> at about 550 °C. Moreover, then, the effect of calcination temperature on the catalyst properties was studied using XRD, BET, and TPR characterizations. It can be known that with the increase in calcination temperature, the LaNiO<sub>3</sub> crystal phase tends to be more perfect, and the occurrence of the sintering phenomenon could cause a larger LaNiO<sub>3</sub> particle size and a smaller specific surface area. The increasing reduction difficulty results in smaller Ni<sup>0</sup> grains and a stronger interaction between the support and the metal active component. At the same reaction temperature, the methane conversion increases with increasing calcination temperature before 800 °C, while LNO-C900 shows a certain loss of activity compared with LNO-C800. There is also an optimal value of 1.5 for S/C. Excessive steam will also cause a significant decline in activity. The oxidation of the Ni component was also demonstrated using XRD characterization of spent catalysts when S/C was more than 2. TPO and Raman spectra also show that carbon deposition resistance of the catalysts can be enhanced with the increase in calcination temperature.

**Author Contributions:** Y.W.: investigation, methodology, conceptualization, writing—review and editing, and visualization. S.Q.: methodology and experiment. Y.C. (Yuxin Chen): methodology, experiment, and visualization. B.Y.: methodology and experiment. Y.C. (Yi Cheng): conceptualization, supervision, writing—reviewing and editing, and funding acquisition. All authors have read and agreed to the published version of the manuscript.

**Funding:** This research was funded by the National Natural Science Foundation of China (No. 22008137 and No. 22278235).

**Conflicts of Interest:** The authors declare that they have no known competing financial interests or personal relationships that could have appeared to influence the work reported in this paper.

#### References

- Sehested, J. Four challenges for nickel steam-reforming catalysts. *Catal. Today* **2006**, *111*, 103–110. [[CrossRef](#)]
- Meloni, E.; Martino, M.; Palma, V. A Short Review on Ni Based Catalysts and Related Engineering Issues for Methane Steam Reforming. *Catalysts* **2020**, *10*, 352. [[CrossRef](#)]
- Pashchenko, D.; Makarov, I. Carbon deposition in steam methane reforming over a Ni-based catalyst: Experimental and thermodynamic analysis. *Energy* **2021**, *222*, 119993. [[CrossRef](#)]
- Garba, Z.N.; Zhou, W.; Zhang, M.; Yuan, Z. A review on the preparation, characterization and potential application of perovskites as adsorbents for wastewater treatment. *Chemosphere* **2020**, *244*, 125474. [[CrossRef](#)] [[PubMed](#)]

5. Fierro, J.L.G. Hydrogenation of Carbon Oxides over Perovskite-Type Oxides. *Catal. Rev.* **1992**, *34*, 321–336. [[CrossRef](#)]
6. Singh, U.G.; Li, J.; Bennett, J.W.; Rappe, A.M.; Seshadri, R.; Scott, S.L. A Pd-doped perovskite catalyst,  $\text{BaCe}_{1-x}\text{Pd}_x\text{O}_{3-\delta}$ , for CO oxidation. *J. Catal.* **2007**, *249*, 349–358. [[CrossRef](#)]
7. Seiyama, T. Total Oxidation of Hydrocarbons on Perovskite Oxides. *Catal. Rev.* **1992**, *34*, 281–300. [[CrossRef](#)]
8. Zhang, R.; Alamdari, H.; Kaliaguine, S.  $\text{SO}_2$  poisoning of  $\text{LaFe}_{0.8}\text{Cu}_{0.2}\text{O}_3$  perovskite prepared by reactive grinding during NO reduction by  $\text{C}_3\text{H}_6$ . *Appl. Catal. A Gen.* **2008**, *340*, 140–151. [[CrossRef](#)]
9. Zhu, J.; Thomas, A. Perovskite-type mixed oxides as catalytic material for NO removal. *Appl. Catal. B Environ.* **2009**, *92*, 225–233. [[CrossRef](#)]
10. Zhu, J.; Li, H.; Zhong, L.; Xiao, P.; Xu, X.; Yang, X.; Zhao, Z.; Li, J. Perovskite Oxides: Preparation, Characterizations, and Applications in Heterogeneous Catalysis. *ACS Catal.* **2014**, *4*, 2917–2940. [[CrossRef](#)]
11. Shao, Z.; Zhou, W.; Zhu, Z. Advanced synthesis of materials for intermediate-temperature solid oxide fuel cells. *Prog. Mater. Sci.* **2012**, *57*, 804–874. [[CrossRef](#)]
12. Royer, S.; Duprez, D.; Can, F.; Courtois, X.; Batiot-Dupeyrat, C.; Laassiri, S.; Alamdari, H. Perovskites as Substitutes of Noble Metals for Heterogeneous Catalysis: Dream or Reality. *Chem. Rev.* **2014**, *114*, 10292–10368. [[CrossRef](#)]
13. Maneerung, T.; Hidajat, K.; Kawi, S.  $\text{LaNiO}_3$  perovskite catalyst precursor for rapid decomposition of methane: Influence of temperature and presence of  $\text{H}_2$  in feed stream. *Catal. Today* **2011**, *171*, 24–35. [[CrossRef](#)]
14. Batiot-Dupeyrat, C.; Valderrama, G.; Meneses, A.; Martinez, F.; Barrault, J.; Tatibouët, J.M. Pulse study of  $\text{CO}_2$  reforming of methane over  $\text{LaNiO}_3$ . *Appl. Catal. A Gen.* **2003**, *248*, 143–151. [[CrossRef](#)]
15. Choi, S.O.; Moon, S.H. Performance of  $\text{La}_{1-x}\text{Ce}_x\text{Fe}_{0.7}\text{Ni}_{0.3}\text{O}_3$  perovskite catalysts for methane steam reforming. *Catal. Today* **2009**, *146*, 148–153. [[CrossRef](#)]
16. Valderrama, G.; Kiennemann, A.; Goldwasser, M.R. La-Sr-Ni-Co-O based perovskite-type solid solutions as catalyst precursors in the  $\text{CO}_2$  reforming of methane. *J. Power Sources* **2010**, *195*, 1765–1771. [[CrossRef](#)]
17. Villoria, J.-A.; Mota, N.; Al-Sayari, S.; Álvarez-Galván, M.-C. Perovskites as catalysts in the reforming of hydrocarbons: A review. *Micro Nanosyst.* **2012**, *4*, 231–252. [[CrossRef](#)]
18. Yang, Q.; Liu, G.; Liu, Y. Perovskite-Type Oxides as the Catalyst Precursors for Preparing Supported Metallic Nanocatalysts: A Review. *Ind. Eng. Chem. Res.* **2018**, *57*, 1–17. [[CrossRef](#)]
19. Bian, Z.; Wang, Z.; Jiang, B.; Hongmanorom, P.; Zhong, W.; Kawi, S. A review on perovskite catalysts for reforming of methane to hydrogen production. *Renew. Sustain. Energy Rev.* **2020**, *134*, 110291. [[CrossRef](#)]
20. Bhattar, S.; Abedin, M.A.; Kanitkar, S.; Spivey, J.J. A review on dry reforming of methane over perovskite derived catalysts. *Catal. Today* **2021**, *365*, 2–23. [[CrossRef](#)]
21. Pena, M.; Fierro, J. Chemical structures and performance of perovskite oxides. *Chem. Rev.* **2001**, *101*, 1981–2018. [[CrossRef](#)] [[PubMed](#)]
22. Arandiyán, H.; Li, J.; Ma, L.; Hashemnejad, S.M.; Mirzaei, M.Z.; Chen, J.; Chang, H.; Liu, C.; Wang, C.; Chen, L. Methane reforming to syngas over  $\text{LaNi}_x\text{Fe}_{1-x}\text{O}_3$  ( $0 \leq x \leq 1$ ) mixed-oxide perovskites in the presence of  $\text{CO}_2$  and  $\text{O}_2$ . *J. Ind. Eng. Chem.* **2012**, *18*, 2103–2114. [[CrossRef](#)]
23. Jahangiri, A.; Aghabozorg, H.; Pahlavanzadeh, H. Effects of Fe substitutions by Ni in La–Ni–O perovskite-type oxides in reforming of methane with  $\text{CO}_2$  and  $\text{O}_2$ . *Int. J. Hydrog. Energy* **2013**, *38*, 10407–10416. [[CrossRef](#)]
24. Yang, E.-h.; Noh, Y.-s.; Ramesh, S.; Lim, S.S.; Moon, D.J. The effect of promoters in  $\text{La}_{0.9}\text{M}_{0.1}\text{Ni}_{0.5}\text{Fe}_{0.5}\text{O}_3$  ( $\text{M} = \text{Sr}, \text{Ca}$ ) perovskite catalysts on dry reforming of methane. *Fuel Process. Technol.* **2015**, *134*, 404–413. [[CrossRef](#)]
25. Tsoukalou, A.; Imtiaz, Q.; Kim, S.M.; Abdala, P.M.; Yoon, S.; Müller, C.R. Dry-reforming of methane over bimetallic Ni–M/ $\text{La}_2\text{O}_3$  ( $\text{M} = \text{Co}, \text{Fe}$ ): The effect of the rate of  $\text{La}_2\text{O}_2\text{CO}_3$  formation and phase stability on the catalytic activity and stability. *J. Catal.* **2016**, *343*, 208–214. [[CrossRef](#)]
26. Wang, M.; Zhao, T.; Dong, X.; Li, M.; Wang, H. Effects of Ce substitution at the A-site of  $\text{LaNi}_{0.5}\text{Fe}_{0.5}\text{O}_3$  perovskite on the enhanced catalytic activity for dry reforming of methane. *Appl. Catal. B Environ.* **2018**, *224*, 214–221. [[CrossRef](#)]
27. Komarala, E.P.; Komissarov, I.; Rosen, B.A. Effect of Fe and Mn Substitution in  $\text{LaNiO}_3$  on Exsolution, Activity, and Stability for Methane Dry Reforming. *Catalysts* **2019**, *10*, 27. [[CrossRef](#)]
28. Wang, Z.; Wang, C.; Chen, S.; Liu, Y. Co–Ni bimetal catalyst supported on perovskite-type oxide for steam reforming of ethanol to produce hydrogen. *Int. J. Hydrog. Energy* **2014**, *39*, 5644–5652. [[CrossRef](#)]
29. Liu, F.; Qu, Y.; Yue, Y.; Liu, G.; Liu, Y. Nano bimetallic alloy of Ni–Co obtained from  $\text{LaCo}_x\text{Ni}_{1-x}\text{O}_3$  and its catalytic performance for steam reforming of ethanol. *RSC Adv.* **2015**, *5*, 16837–16846. [[CrossRef](#)]
30. Zhao, L.; Han, T.; Wang, H.; Zhang, L.; Liu, Y. Ni–Co alloy catalyst from  $\text{LaNi}_{1-x}\text{Co}_x\text{O}_3$  perovskite supported on zirconia for steam reforming of ethanol. *Appl. Catal. B Environ.* **2016**, *187*, 19–29. [[CrossRef](#)]
31. Kim, W.Y.; Jang, J.S.; Ra, E.C.; Kim, K.Y.; Kim, E.H.; Lee, J.S. Reduced perovskite  $\text{LaNiO}_3$  catalysts modified with Co and Mn for low coke formation in dry reforming of methane. *Appl. Catal. A Gen.* **2019**, *575*, 198–203. [[CrossRef](#)]
32. Kwon, O.; Huang, R.; Cao, T.; Vohs, J.M.; Gorte, R.J. Dry reforming of methane over Ni supported on  $\text{LaMnO}_3$  thin films. *Catal. Today* **2021**, *382*, 142–147. [[CrossRef](#)]
33. Kwon, O.; Foucher, A.C.; Huang, R.; Stach, E.A.; Vohs, J.M.; Gorte, R.J. Evidence for redispersion of Ni on  $\text{LaMnO}_3$  films following high-temperature oxidation. *J. Catal.* **2022**, *407*, 213–220. [[CrossRef](#)]

34. Nishihata, Y.; Mizuki, J.; Akao, T.; Tanaka, H.; Uenishi, M.; Kimura, M.; Okamoto, T.; Hamada, N. Self-regeneration of a Pd-perovskite catalyst for automotive emissions control. *Nature* **2002**, *418*, 164–167. [[CrossRef](#)]
35. Neagu, D.; Oh, T.-S.; Miller, D.N.; Ménard, H.; Bukhari, S.M.; Gamble, S.R.; Gorte, R.J.; Vohs, J.M.; Irvine, J.T.S. Nano-socketed nickel particles with enhanced coking resistance grown in situ by redox exsolution. *Nat. Commun.* **2015**, *6*, 8120. [[CrossRef](#)]
36. Lin, C.; Foucher, A.C.; Stach, E.A.; Gorte, R.J. A Thermodynamic Investigation of Ni on Thin-Film Titanates (ATiO<sub>3</sub>). *Inorganics* **2020**, *8*, 69. [[CrossRef](#)]
37. Mao, X.; Foucher, A.C.; Stach, E.A.; Gorte, R.J. Changes in Ni-NiO equilibrium due to LaFeO<sub>3</sub> and the effect on dry reforming of CH<sub>4</sub>. *J. Catal.* **2020**, *381*, 561–569. [[CrossRef](#)]
38. Pereñíguez, R.; Gonzalez-delaCruz, V.M.; Caballero, A.; Holgado, J.P. LaNiO<sub>3</sub> as a precursor of Ni/La<sub>2</sub>O<sub>3</sub> for CO<sub>2</sub> reforming of CH<sub>4</sub>: Effect of the presence of an amorphous NiO phase. *Appl. Catal. B Environ.* **2012**, *123–124*, 324–332.
39. Rida, K.; Peña, M.A.; Sastre, E.; Martínez-Arias, A. Effect of calcination temperature on structural properties and catalytic activity in oxidation reactions of LaNiO<sub>3</sub> perovskite prepared by Pechini method. *J. Rare Earths* **2012**, *30*, 210–216. [[CrossRef](#)]
40. Haynes, D.J.; Shekhawat, D.; Berry, D.A.; Zondlo, J.; Roy, A.; Spivey, J.J. Characterization of calcination temperature on a Ni-substituted lanthanum-strontium-zirconate pyrochlore. *Ceram. Int.* **2017**, *43*, 16744–16752. [[CrossRef](#)]
41. Liu, L.; Zhang, Z.; Das, S.; Xi, S.; Kawi, S. LaNiO<sub>3</sub> as a precursor of Ni/La<sub>2</sub>O<sub>3</sub> for reverse water-gas shift in DBD plasma: Effect of calcination temperature. *Energy Convers. Manag.* **2020**, *206*, 112475. [[CrossRef](#)]
42. González-Varela, D.; Araiza, D.G.; Díaz, G.; Pfeiffer, H. LaNiO<sub>3</sub> Perovskite Synthesis through the EDTA–Citrate Complexing Method and Its Application to CO Oxidation. *Catalysts* **2022**, *12*, 57. [[CrossRef](#)]
43. Pechini, M. Method of Preparing Lead and Alkaline Earth Titanates and Niobates and Coating Method Using the Same to Form a Capacitor. US Patent No. 3330697A, 11 July 1967.
44. Djani, F.; Omari, M.; Martínez-Arias, A. Synthesis, characterization and catalytic properties of La(Ni,Fe)O<sub>3</sub>–NiO nanocomposites. *J. Sol.-Gel Sci. Technol.* **2015**, *78*, 1–10. [[CrossRef](#)]
45. Devi, P.S.; Rao, M.S. Study of the thermal decomposition of lanthanum and chromium citrate hydrates. *J. Anal. Appl. Pyrolysis* **1992**, *22*, 187–195. [[CrossRef](#)]
46. Wang, H.; Zhu, Y.; Liu, P.; Yao, W. Preparation of nanosized perovskite LaNiO<sub>3</sub> powder via amorphous heteronuclear complex precursor. *J. Mater. Sci.* **2003**, *38*, 1939–1943. [[CrossRef](#)]
47. Fernandes, J.D.G.; Melo, D.M.A.; Zinner, L.B.; Salustiano, C.M.; Silva, Z.R.; Martinelli, A.E.; Cerqueira, M.; Alves Júnior, C.; Longo, E.; Bernardi, M.I.B. Low-temperature synthesis of single-phase crystalline LaNiO<sub>3</sub> perovskite via Pechini method. *Mater. Lett.* **2002**, *53*, 122–125. [[CrossRef](#)]
48. Fjellvåg, H.; Hansteen, O.H.; Tilset, B.G.; Olafsen, A.; Sakai, N.; Seim, H. Thermal analysis as an aid in the synthesis of non-stoichiometric perovskite type oxides. *Thermochim. Acta* **1995**, *256*, 75–89. [[CrossRef](#)]
49. Dreyer, M.; Krebs, M.; Najafshirtari, S.; Rabe, A.; Friedel Ortega, K.; Behrens, M. The Effect of Co Incorporation on the CO Oxidation Activity of LaFe<sub>1-x</sub>Co<sub>x</sub>O<sub>3</sub> Perovskites. *Catalysts* **2021**, *11*, 550. [[CrossRef](#)]
50. Wang, Y.; Zhu, J.; Yang, X.; Lu, L.; Wang, X. Preparation and characterization of LaNiO<sub>3</sub> nanocrystals. *Mater. Res. Bull.* **2006**, *41*, 1565–1570. [[CrossRef](#)]
51. Le, N.T.H.; Calderón-Moreno, J.M.; Popa, M.; Crespo, D.; Van Hong, L.; Phuc, N.X. LaNiO<sub>3</sub> nanopowder prepared by an ‘amorphous citrate’ route. *J. Eur. Ceram. Soc.* **2006**, *26*, 403–407. [[CrossRef](#)]
52. Valderrama, G.; Goldwasser, M.R.; Navarro, C.U.D.; Tatibouët, J.M.; Barrault, J.; Batiot-Dupeyrat, C.; Martínez, F. Dry reforming of methane over Ni perovskite type oxides. *Catal. Today* **2005**, *107–108*, 785–791.
53. Santos, D.B.L.; Noronha, F.B.; Hori, C.E. Bi-reforming of methane for hydrogen production using LaNiO<sub>3</sub>/Ce<sub>x</sub>Zr<sub>1-x</sub>O<sub>2</sub> as precursor material. *Int. J. Hydrog. Energy* **2020**, *45*, 13947–13959. [[CrossRef](#)]
54. Ramon, A.P.; Li, X.; Clark, A.H.; Safonova, O.V.; Marcos, F.C.; Assaf, E.M.; van Bokhoven, J.A.; Artiglia, L.; Assaf, J.M. In situ study of low-temperature dry reforming of methane over La<sub>2</sub>Ce<sub>2</sub>O<sub>7</sub> and LaNiO<sub>3</sub> mixed oxides. *Appl. Catal. B Environ.* **2022**, *315*, 121528. [[CrossRef](#)]
55. Ruckenstein, E.; Hu, Y. Interactions between Ni and La<sub>2</sub>O<sub>3</sub> in Ni/La<sub>2</sub>O<sub>3</sub> Catalysts Prepared Using Different Ni Precursors. *J. Catal.* **1996**, *161*, 55–61. [[CrossRef](#)]
56. Cesteros, Y.; Salagre, P.; Medina, F.; Sueiras, J.E. Preparation and Characterization of Several High-Area NiAl<sub>2</sub>O<sub>4</sub> Spinel. Study of Their Reducibility. *Chem. Mater.* **2000**, *12*, 331–335. [[CrossRef](#)]
57. Courson, C.; Udron, L.; Świerczyński, D.; Petit, C.; Kiennemann, A. Hydrogen production from biomass gasification on nickel catalysts: Tests for dry reforming of methane. *Catal. Today* **2002**, *76*, 75–86. [[CrossRef](#)]
58. Han, B.; Zhao, L.; Wang, F.; Xu, L.; Yu, H.; Cui, Y.; Zhang, J.; Shi, W. Effect of Calcination Temperature on the Performance of the Ni@SiO<sub>2</sub> Catalyst in Methane Dry Reforming. *Ind. Eng. Chem. Res.* **2020**, *59*, 13370–13379. [[CrossRef](#)]
59. Vella, L.D.; Villoria, J.A.; Specchia, S.; Mota, N.; Fierro, J.L.G.; Specchia, V. Catalytic partial oxidation of CH<sub>4</sub> with nickel–lanthanum-based catalysts. *Catal. Today* **2011**, *171*, 84–96. [[CrossRef](#)]
60. Kuras, M.; Roucou, R.; Petit, C. Studies of LaNiO<sub>3</sub> used as a precursor for catalytic carbon nanotubes growth. *J. Mol. Catal. A Chem.* **2007**, *265*, 209–217. [[CrossRef](#)]
61. Rabelo-Neto, R.C.; Sales, H.B.E.; Inocência, C.V.M.; Varga, E.; Oszko, A.; Erdohelyi, A.; Noronha, F.B.; Mattos, L.V. CO<sub>2</sub> reforming of methane over supported LaNiO<sub>3</sub> perovskite-type oxides. *Appl. Catal. B Environ.* **2018**, *221*, 349–361. [[CrossRef](#)]

62. Santos, M.d.S.; Neto, R.C.R.; Noronha, F.B.; Bargiela, P.; Rocha, M.d.G.C.d.; Resini, C.; Carbó-Argibay, E.; Fréty, R.; Brandão, S.T. Perovskite as catalyst precursors in the partial oxidation of methane: The effect of cobalt, nickel and pretreatment. *Catal. Today* **2018**, *299*, 229–241. [[CrossRef](#)]
63. Kuras, M.; Zimmermann, Y.; Petit, C. Reactivity of perovskite-type precursor in MWCNTs synthesis. *Catal. Today* **2008**, *138*, 55–61. [[CrossRef](#)]
64. Da Silva, A.A.A.; da Costa, L.O.O.; Mattos, L.V.; Noronha, F.B. The study of the performance of Ni-based catalysts obtained from LaNiO<sub>3</sub> perovskite-type oxides synthesized by the combustion method for the production of hydrogen by reforming of ethanol. *Catal. Today* **2013**, *213*, 25–32. [[CrossRef](#)]
65. Batiot-Dupeyrat, C.; Gallego, G.A.S.; Mondragon, F.; Barrault, J.; Tatibouët, J.-M. CO<sub>2</sub> reforming of methane over LaNiO<sub>3</sub> as precursor material. *Catal. Today* **2005**, *107–108*, 474–480. [[CrossRef](#)]
66. Sierra Gallego, G.; Batiot-Dupeyrat, C.; Barrault, J.; Mondragón, F. Dual Active-Site Mechanism for Dry Methane Reforming over Ni/La<sub>2</sub>O<sub>3</sub> Produced from LaNiO<sub>3</sub> Perovskite. *Ind. Eng. Chem. Res.* **2008**, *47*, 9272–9278. [[CrossRef](#)]
67. He, L.; Ren, Y.; Yue, B.; Tsang, S.C.E.; He, H. Tuning Metal–Support Interactions on Ni/Al<sub>2</sub>O<sub>3</sub> Catalysts to Improve Catalytic Activity and Stability for Dry Reforming of Methane. *Processes* **2021**, *9*, 706. [[CrossRef](#)]
68. Wang, Y.-H.; Liu, H.-M.; Xu, B.-Q. Durable Ni/MgO catalysts for CO<sub>2</sub> reforming of methane: Activity and metal–support interaction. *J. Mol. Catal. A Chem.* **2009**, *299*, 44–52. [[CrossRef](#)]
69. Gallego, G.S.; Mondragón, F.; Barrault, J.; Tatibouët, J.-M.; Batiot-Dupeyrat, C. CO<sub>2</sub> reforming of CH<sub>4</sub> over La–Ni based perovskite precursors. *Appl. Catal. A Gen.* **2006**, *311*, 164–171. [[CrossRef](#)]
70. Mosayebi, A.; Nasabi, M. Steam methane reforming on LaNiO<sub>3</sub> perovskite-type oxide for syngas production, activity tests, and kinetic modeling. *Int. J. Energy Res.* **2020**, *44*, 5500–5515. [[CrossRef](#)]
71. Lutz, A.E.; Bradshaw, R.W.; Keller, J.O.; Witmer, D.E. Thermodynamic analysis of hydrogen production by steam reforming. *Int. J. Hydrog. Energy* **2003**, *28*, 159–167. [[CrossRef](#)]
72. Carapellucci, R.; Giordano, L. Steam, dry and autothermal methane reforming for hydrogen production: A thermodynamic equilibrium analysis. *J. Power Sources* **2020**, *469*, 228391. [[CrossRef](#)]
73. Rostrup-Nielsen, J.R.; Sehested, J.; Nørskov, J.K. Hydrogen and Synthesis Gas by Steam and CO<sub>2</sub> Reforming. In *Advances in Catalysis*; Academic Press: Cambridge, MA, USA, 2002; Volume 47, pp. 65–139.
74. Rostrup-Nielsen, J.; Nørskov, J.K. Step sites in syngas catalysis. *Top. Catal.* **2006**, *40*, 45–48. [[CrossRef](#)]
75. Wei, J.; Iglesia, E. Structural requirements and reaction pathways in methane activation and chemical conversion catalyzed by rhodium. *J. Catal.* **2004**, *225*, 116–127. [[CrossRef](#)]
76. Hoang, D.L.; Chan, S.H.; Ding, O.L. Kinetic and modelling study of methane steam reforming over sulfide nickel catalyst on a gamma alumina support. *Chem. Eng. J.* **2005**, *112*, 1–11. [[CrossRef](#)]
77. Hou, K.; Hughes, R. The kinetics of methane steam reforming over a Ni/ $\alpha$ -Al<sub>2</sub>O catalyst. *Chem. Eng. J.* **2001**, *82*, 311–328. [[CrossRef](#)]
78. Rostrup-Nielsen, J.R. Production of synthesis gas. *Catal. Today* **1993**, *18*, 305–324. [[CrossRef](#)]
79. Aparicio, L.M. Transient Isotopic Studies and Microkinetic Modeling of Methane Reforming over Nickel Catalysts. *J. Catal.* **1997**, *165*, 262–274. [[CrossRef](#)]
80. Mickevičius, S.; Grebinskij, S.; Bondarenka, V.; Vengalis, B.; Šliužienė, K.; Orłowski, B.A.; Osinniy, V.; Drube, W. Investigation of epitaxial LaNiO<sub>3-x</sub> thin films by high-energy XPS. *J. Alloys Compd.* **2006**, *423*, 107–111. [[CrossRef](#)]
81. Serrano-Lotina, A.; Rodríguez, L.; Muñoz, G.; Martín, A.J.; Folgado, M.A.; Daza, L. Biogas reforming over La-NiMgAl catalysts derived from hydrotalcite-like structure: Influence of calcination temperature. *Catal. Commun.* **2011**, *12*, 961–967. [[CrossRef](#)]
82. Abbas, S.Z.; Dupont, V.; Mahmud, T. Kinetics study and modelling of steam methane reforming process over a NiO/Al<sub>2</sub>O<sub>3</sub> catalyst in an adiabatic packed bed reactor. *Int. J. Hydrog. Energy* **2017**, *42*, 2889–2903. [[CrossRef](#)]
83. Imran, U.; Ahmad, A.; Othman, M. Kinetic Based Simulation of Methane Steam Reforming and Water Gas Shift for Hydrogen Production Using Aspen Plus. *Chem. Eng. Trans.* **2017**, *56*, 1681.
84. Helveg, S.; López-Cartes, C.; Sehested, J.; Hansen, P.L.; Clausen, B.S.; Rostrup-Nielsen, J.R.; Abild-Pedersen, F.; Nørskov, J.K. Atomic-scale imaging of carbon nanofibre growth. *Nature* **2004**, *427*, 426–429. [[CrossRef](#)]
85. Sierra Gallego, G.; Mondragón, F.; Tatibouët, J.-M.; Barrault, J.; Batiot-Dupeyrat, C. Carbon dioxide reforming of methane over La<sub>2</sub>NiO<sub>4</sub> as catalyst precursor—Characterization of carbon deposition. *Catal. Today* **2008**, *133–135*, 200–209. [[CrossRef](#)]
86. Hufschmidt, D.; Bobadilla, L.F.; Romero-Sarria, F.; Centeno, M.A.; Odriozola, J.A.; Montes, M.; Falabella, E. Supported nickel catalysts with a controlled molecular architecture for the catalytic reformation of methane. *Catal. Today* **2010**, *149*, 394–400. [[CrossRef](#)]
87. Abasaheed, A.; Kasim, S.; Khan, W.; Sofiu, M.; Ibrahim, A.; Fakeeha, A.; Al-Fatesh, A. Hydrogen Yield from CO<sub>2</sub> Reforming of Methane: Impact of La<sub>2</sub>O<sub>3</sub> Doping on Supported Ni Catalysts. *Energies* **2021**, *14*, 2412. [[CrossRef](#)]
88. Liu, B.S.; Au, C.T. Carbon deposition and catalyst stability over La<sub>2</sub>NiO<sub>4</sub>/ $\gamma$ -Al<sub>2</sub>O<sub>3</sub> during CO<sub>2</sub> reforming of methane to syngas. *Appl. Catal. A Gen.* **2003**, *244*, 181–195. [[CrossRef](#)]
89. Habibi, N.; Rezaei, M.; Majidian, N.; Andache, M. CH<sub>4</sub> reforming with CO<sub>2</sub> for syngas production over La<sub>2</sub>O<sub>3</sub> promoted Ni catalysts supported on mesoporous nanostructured lambda-Al<sub>2</sub>O<sub>3</sub>. *J. Energy Chem.* **2014**, *23*, 435–442. [[CrossRef](#)]

90. Bicki, R.; Antoniak-Jurak, K.; Michalska, K.; Franczyk, E.; Konkol, M.; Kowalik, P.; Panczyk, M.; Ryczkowski, J.; Slowik, G.; Borowiecki, T. The effect of  $\text{La}_2\text{O}_3$  and  $\text{CeO}_2$  modifiers on properties of Ni-Al catalysts for LNG prereforming. *Int. J. Hydrog. Energy* **2021**, *46*, 11664–11676. [[CrossRef](#)]
91. Tuza, P.V.; Souza, M.M.V.M. Steam Reforming of Methane Over Catalyst Derived from Ordered Double Perovskite: Effect of Crystalline Phase Transformation. *Catal. Lett.* **2015**, *146*, 47–53. [[CrossRef](#)]
92. Provendier, H.; Petit, C.; Roger, A.C.; Kiennemann, A. Influence of the Precursors on the Formation of a Trimetallic Defined Structure. Application on Ni Catalysts Used for Syngas Obtention. *Stud. Surf. Sci. Catal.* **1998**, *118*, 285–294.
93. De Lima, S.M.; da Silva, A.M.; da Costa, L.O.O.; Assaf, J.M.; Jacobs, G.; Davis, B.H.; Mattos, L.V.; Noronha, F.B. Evaluation of the performance of Ni/ $\text{La}_2\text{O}_3$  catalyst prepared from  $\text{LaNiO}_3$  perovskite-type oxides for the production of hydrogen through steam reforming and oxidative steam reforming of ethanol. *Appl. Catal. A Gen.* **2010**, *377*, 181–190. [[CrossRef](#)]

**Disclaimer/Publisher's Note:** The statements, opinions and data contained in all publications are solely those of the individual author(s) and contributor(s) and not of MDPI and/or the editor(s). MDPI and/or the editor(s) disclaim responsibility for any injury to people or property resulting from any ideas, methods, instructions or products referred to in the content.